Supplementary Information for 'Harmonic Control of Dynamical Freezing in Programmable Rydberg Atom Arrays'

Madhumita Sarkar,[1,*] Ben Zindorf,[1,*] Bhaskar Mukherjee,[2,1] Sougato Bose,[1] and Roopayan Ghosh[1,3,†]

[1] *Department of Physics and Astronomy, University College London, Gower Street, WC1E 6BT, London, United Kingdom.*
[2] *Department of Physics, S.N. Bose Centre for Basic Sciences, Kolkata, 700106, India.*
[3] *School of Basic Sciences, Indian Institute of Technology, Bhubaneswar, 752050, India.*

I. RESOLVING INTERFERENCE WITHIN INDIVIDUAL DRIVE CYCLES

The frequency-dependent vacuum freezing raises a fundamental question: how do quantum phases interfere across repeated passages to produce dynamical stability? To probe this microscopically, we track the time-resolved Rydberg population within a single drive cycle in 100-atom chains on Aquila (Fig. 1), benchmarked against Bloqade simulations at $L = 14$.

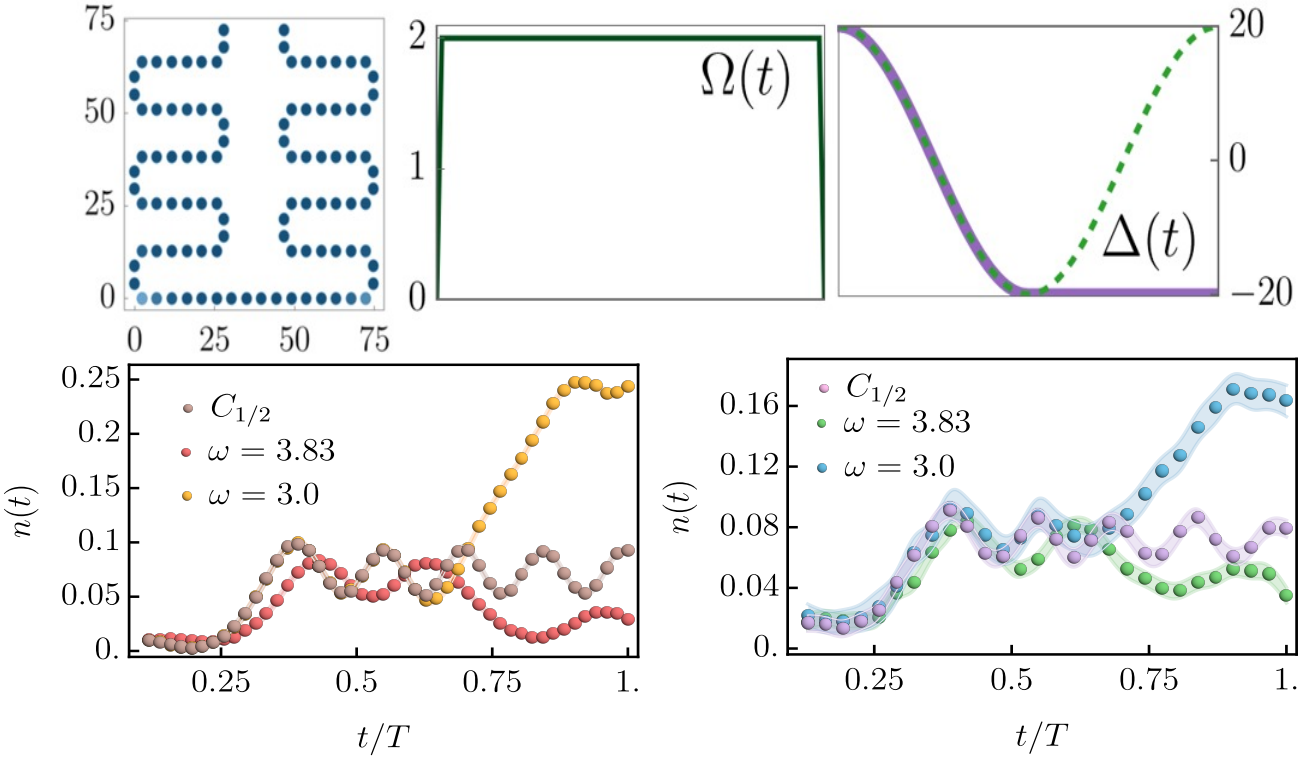

FIG. 1. **Microscopic dynamics within a drive cycle.** Time-resolved measurements reveal how Stückelberg interference produces vacuum-state freezing. **Top:** Experimental geometry and drive protocol. The purple line indicates the half-cycle control sequence, where the detuning is held fixed beyond $t = T/2$, $\Delta(t > T/2) = \Delta(T/2)$. **Left:** Classical simulations using Bloqade ($L = 14$) comparing constructive ($\omega = 3.0$, yellow) and destructive ($\omega = 3.83$, red) interference. Brown circles denote the half-cycle protocol ($C_{1/2}$), which shows only residual oscillations and no interference signature. **Right:** Experimental verification on Aquila ($L = 100$) at the same frequencies. The clear contrast between full-cycle (red/green and yellow/blue) and half-cycle (brown/purple) dynamics demonstrates that vacuum freezing arises from coherent amplitude recombination via second passage through the avoided crossing, rather than from an individual passage.

* These authors contributed equally to this work
† roopayan@iitbbs.ac.in

At frequencies yielding destructive interference ($\omega \sim 3.825$ rad/μs), the excitation probability rises approaching the first avoided crossing but falls during the second, completing the cycle with $n(T) < 3\%$—near-perfect vacuum recovery. In contrast, at constructive frequencies ($\omega \sim 3.0$ rad/μs), excitations accumulate coherently across both traversals, leading to final densities exceeding 15%.

To confirm that interference requires completion of the full temporal loop, we implement a truncated protocol halting evolution at half-period ($t = T/2$), keeping Δ fixed thereafter. In this case, the characteristic contrast vanishes. Excitation grows monotonically and settles into residual oscillations, demonstrating that the observed freezing originates from phase recombination across the full cycle, not from single-pass dynamics.

These time-resolved measurements directly visualize the Stückelberg mechanism at the many-body level. By resolving constructive and destructive recombination within each drive cycle of a 100-atom ensemble, our results establish temporal interference as a coherent, scalable mechanism underlying Floquet control in interacting quantum systems.

II. INTERFERENCE AFTER MULTIPLE DRIVE CYCLES

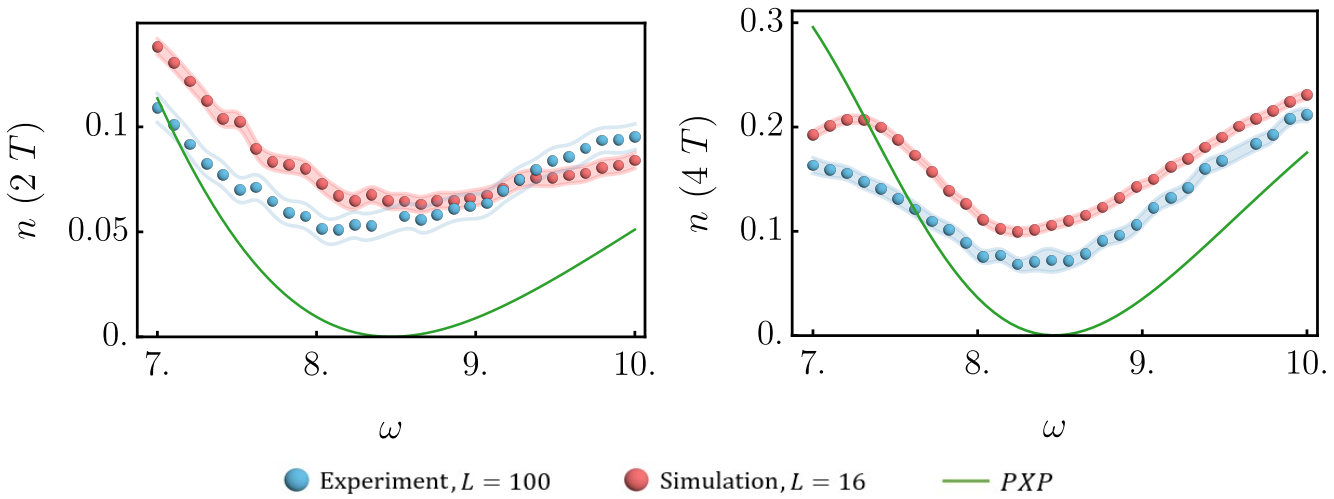

FIG. 2. Average Rydberg excitation density n vs frequency ω after Left: two drive cycles, Right: four drive cycles

In this section we report the excitation density under repeated periodic driving. To remain within the experimentally accessible coherence time, we consider higher drive frequencies than in the main text and focus on parameters near the first (smallest) zero of the Bessel function J_0. Since the argument of J_0 scales as Δ_0/ω, this corresponds to the highest drive frequency at which the characteristic interference minima remain observable in our experiment. We experimentally measure the excitation density for $L = 100$ atoms in a snake geometry after two and four drive cycles, shown in Fig. 2 (left and right panels, respectively), and compare these results with numerical simulations obtained using Bloqade for a system of size $L = 14$, as well as with the constrained PXP model at the same size.

While temporal interference persists over multiple cycles, its visibility is significantly reduced with increasing drive duration. In particular, the excitation density at points of constructive interference is markedly higher after four cycles than after two, indicating the onset of Floquet heating. This behavior is captured both in experiment and in the full Rydberg simulations, consistent with the understanding that dynamical freezing in interacting Floquet systems is generally a transient prethermal regime rather than a truly stable phase, in line with recent theoretical studies attributing such heating processes to instanton-mediated mechanisms [1].

By contrast, the PXP model exhibits substantially weaker degradation of interference visibility over the same timescales, reflecting its effectively constrained and non-generic interaction structure. This comparison highlights that finite-range interaction tails play a central role in enabling genuine many-body dynamics and in determining the long-time stability of driven interference phenomena. In this sense, the extended interactions present in realistic Rydberg systems are not merely a perturbation to constrained models but are essential for capturing the experimentally observed heating and coherence properties.

III. THE FLOQUET PERTURBATION EXPANSION

In the main text we define, For our driven Rydberg system, we define, $H(t) = H_0(t) + H_1$, with

$$H_0(t) = \Delta_0 \cos(\omega t) \sum_i n_i + \sum_{j \in \mathrm{LR}(i)} V_{ij}\, n_i n_j, \tag{1}$$

$$H_1 = \Omega \sum_i \tilde{\sigma}_i^x. \tag{2}$$

The Floquet perturbation expansion proceeds analogously to a Dyson series formulated in the interaction picture [2]. The zeroth-order term defines the unperturbed evolution operator

$$U_0(T,0) = e^{-iH_F^{(0)}T} = \mathcal{T} \exp\left[-i \int_0^T H_0(t)\, dt\right], \tag{3}$$

where $\mathcal{T}$ denotes time ordering. Since $H_0(t)$ is diagonal at all times, the corresponding zeroth-order evolution operator is obtained exactly as

$$U_0(t) = \exp\left[-i \frac{\Delta_0}{\omega} \sin(\omega t) \sum_i n_i\right] \exp\left[-it \sum_{j \in \mathrm{LR}(i)} V_{ij}\, n_i n_j\right]. \tag{4}$$

The zeroth-order contribution to the Floquet Hamiltonian arises from the evolution operator $U_0(T)$ over one driving period. Since $\sin(\omega T) = 0$ for $T = 2\pi/\omega$, the contribution from the time-dependent detuning vanishes over a full period, and one finds

$$U_0(T) = \exp\left[-iT \sum_{j \in \mathrm{LR}(i)} V_{ij}\, n_i n_j\right]. \tag{5}$$

This defines the zeroth-order Floquet Hamiltonian

$$H_F^{(0)} = \sum_{j \in \mathrm{LR}(i)} V_{ij}\, n_i n_j, \tag{6}$$

which corresponds to the static interaction energy within the blockade-constrained Hilbert space.

To calculate the first order term, we start from the interaction-picture Hamiltonian

$$H_I(t) = U_0^\dagger(t) H_1 U_0(t), \tag{7}$$

which takes the form

$$H_I(t) = \Omega \sum_i \left[\tilde{\sigma}_i^+ e^{+i\phi_i(t)} + \tilde{\sigma}_i^- e^{-i\phi_i(t)}\right], \tag{8}$$

with

$$\phi_i(t) = \alpha_i t + \frac{\Delta_0}{\omega} \sin(\omega t), \qquad \alpha_i = \sum_{j \in \mathrm{LR}(i)} V_{ij}\, n_j. \tag{9}$$

Here $\tilde{\sigma}_i^\pm$ are projected spin-flip operators acting within the blockade subspace. The quantity α_i is diagonal in the occupation-number basis and therefore commutes with itself at different times, allowing it to be treated as a c-number within the time integral. The effective Floquet Hamiltonian H_F is then defined in the interaction frame generated by $U_0(t)$. Transforming back to the laboratory frame yields $U(T) = U_0(T) e^{-iH_F T}$, where $U_0(T)$ is diagonal in the occupation basis and contributes only configuration-dependent phases, leaving the effective coupling structure unchanged.

First-order Dyson expansion

The time-evolution operator in the interaction picture is

$$U_I(T) = \mathcal{T} \exp\left(-i \int_0^T H_I(t)\, dt \right), \tag{10}$$

where $\mathcal{T}$ denotes time ordering. To first order in the Dyson expansion, this reduces to

$$U_I(T) \simeq \mathbb{I} - i \int_0^T H_I(t)\, dt. \tag{11}$$

The effective Floquet Hamiltonian at this order is defined through

$$U_I(T) \equiv e^{-iH_F^{(1)}T}, \tag{12}$$

which yields

$$H_F^{(1)} = \frac{1}{T} \int_0^T H_I(t)\, dt, \qquad T = \frac{2\pi}{\omega}. \tag{13}$$

Substituting Eq. (8) into Eq. (13) gives

$$H_F^{(1)} = \Omega \sum_i \left[\tilde{\sigma}_i^+ \mathcal{I}(\alpha_i) + \tilde{\sigma}_i^- \mathcal{I}^*(\alpha_i) \right], \tag{14}$$

where

$$\mathcal{I}(\alpha) = \frac{1}{T} \int_0^T dt\; e^{i[\alpha t + (\Delta_0/\omega)\sin(\omega t)]}. \tag{15}$$

Evaluation of the time integral

To evaluate Eq. (15), we employ the Jacobi–Anger expansion

$$e^{iz\sin\theta} = \sum_{n=-\infty}^{\infty} J_n(z)\, e^{in\theta}. \tag{16}$$

This allows us to write

$$e^{i(\Delta_0/\omega)\sin(\omega t)} = \sum_{n=-\infty}^{\infty} J_n(\Delta_0/\omega)\, e^{in\omega t}. \tag{17}$$

Substituting into Eq. (15), we obtain

$$\mathcal{I}(\alpha) = \frac{1}{T} \sum_{n=-\infty}^{\infty} J_n(\Delta_0/\omega) \int_0^T dt\; e^{i(\alpha+n\omega)t}. \tag{18}$$

The remaining time integral can be evaluated explicitly as

$$\int_0^T dt\, e^{i(\alpha+n\omega)t} = \frac{e^{i(\alpha+n\omega)T} - 1}{i(\alpha+n\omega)}. \tag{19}$$

Using $T = 2\pi/\omega$ and the identity $e^{in\omega T} = e^{i2\pi n} = 1$, this simplifies to

$$\int_0^T dt\, e^{i(\alpha+n\omega)t} = \frac{e^{i2\pi\alpha/\omega} - 1}{i(\alpha+n\omega)}. \tag{20}$$

Combining terms yields the closed-form expression

$$\mathcal{I}(\alpha) = \left(e^{i2\pi\alpha/\omega} - 1\right) \sum_{n=-\infty}^{\infty} \frac{J_n(\Delta_0/\omega)}{iT(\alpha+n\omega)}, \tag{21}$$

which corresponds to Eq. (12) in the main text.

Physical interpretation

Since α_i depends only on occupations outside the blockade radius, the coefficient $\mathcal{I}(\alpha_i)$ conditions the spin-flip dynamics at site i on the surrounding Rydberg configuration. The resulting effective Hamiltonian therefore describes density-assisted spin-flip processes arising from interaction tails beyond the blockade radius.

In the absence of interactions beyond the blockade radius ($V_{ij} = 0$), Eqs. (6) and (14) reduce to $H_F^{(0)} = 0$ and $H_F^{(1)} = \Omega J_0(\Delta_0/\omega) \sum_i \tilde{\sigma}_i^x$. This limit corresponds to the PXP model, which retains only constrained coherent spin flips and neglects interaction-induced corrections arising beyond the blockade radius.

Small-interaction expansion of the Floquet Hamiltonian

We now consider the regime in which interactions beyond the blockade radius are weak but finite,

$$\Omega \sim V_{ij} \sim \omega \ll \Delta_0, \tag{22}$$

which allows us to expose the effect of interaction tails while remaining controlled by the large detuning scale. In this limit, interaction-induced corrections arise in the effective Floquet Hamiltonian that are absent in the PXP model.

Up to first order in the interaction-picture Dyson expansion, the effective Floquet Hamiltonian can be written as

$$H_F = H_F^{(0)} + H_F^{(1)} + O\left(\frac{\Omega V^2}{\Delta_0^2}\right), \tag{23}$$

where the zeroth-order contribution originates entirely from the diagonal part of the Hamiltonian retained in $U_0(t)$,

$$H_F^{(0)} = \sum_i \sum_{j \in \mathrm{LR}(i)} V_{ij}\, n_i n_j. \tag{24}$$

The first-order contribution $H_F^{(1)}$ arises from the time average of the interaction-picture Hamiltonian and is controlled by the coefficient

$$\mathcal{I}(\alpha) = \frac{1}{T} \int_0^T dt\; e^{i[\alpha t + (\Delta_0/\omega)\sin(\omega t)]}. \tag{25}$$

In the present regime, the interaction-induced shift

$$\alpha_i = \sum_{j \in \mathrm{LR}(i)} V_{ij}\, n_j \tag{26}$$

satisfies $|\alpha_i| \ll \Delta_0$, allowing $\mathcal{I}(\alpha_i)$ to be expanded perturbatively in α_i.

Using the Jacobi–Anger expansion and expanding the integrand to linear order in α_i, we obtain

$$\begin{aligned} \mathcal{I}(\alpha_i) &= \frac{1}{T} \int_0^T dt\; e^{i(\Delta_0/\omega)\sin(\omega t)} \left(1 + i\alpha_i t + O(\alpha_i^2)\right) \\ &= \frac{1}{T} \int_0^T dt\; e^{i(\Delta_0/\omega)\sin(\omega t)} + \frac{i\alpha_i}{T} \int_0^T dt\; t\, e^{i(\Delta_0/\omega)\sin(\omega t)} + O(\alpha_i^2). \end{aligned} \tag{27}$$

The first term evaluates to the zeroth-order Bessel function,

$$\frac{1}{T} \int_0^T dt\; e^{i(\Delta_0/\omega)\sin(\omega t)} = J_0(\Delta_0/\omega), \tag{28}$$

while the second term can be evaluated by inserting the Jacobi–Anger expansion and performing the time integral term by term, yielding

$$\frac{i}{T} \int_0^T dt\; t\, e^{i(\Delta_0/\omega)\sin(\omega t)} = \sum_{n \neq 0} \frac{J_n(\Delta_0/\omega)}{n\omega}. \tag{29}$$

Combining these results, the coefficient $\mathcal{I}(\alpha_i)$ admits the expansion

$$\mathcal{I}(\alpha_i) = J_0(\Delta_0/\omega) + \alpha_i \sum_{n\neq 0} \frac{J_n(\Delta_0/\omega)}{n\omega} + O\left(\frac{V^2}{\Delta_0^2}\right). \tag{30}$$

Substituting this expression into the first-order Floquet Hamiltonian yields

$$H_F^{(1)} = \Omega J_0(\Delta_0/\omega) \sum_i \tilde{\sigma}_i^x \quad + \Omega \sum_i \left(\sum_{j\in \mathrm{LR}(i)} \lambda_{ij}\, n_j \right) \tilde{\sigma}_i^x, \tag{31}$$

where the interaction-induced coupling is given by

$$\lambda_{ij} = \frac{V_{ij}}{\omega} \sum_{n\neq 0} \frac{J_n(\Delta_0/\omega)}{n}. \tag{32}$$

This expression makes explicit that, even for weak interaction tails, the effective Floquet Hamiltonian acquires density-assisted spin-flip terms that are absent in the PXP model and arise solely from interactions beyond the blockade radius.

The leading interaction-induced correction therefore corresponds to a density-assisted spin-flip process: a spin at site i can flip only in the presence of a finite interaction-induced energy shift generated by Rydberg excitations at neighbouring sites beyond the blockade radius. In this regime, interactions do not merely renormalize the global flip amplitude, but condition local spin dynamics on the surrounding Rydberg configuration. Such density-assisted processes are absent in the PXP model and provide the leading correction required to capture the experimentally observed dynamics when interactions beyond the blockade radius are retained.

Dual-frequency drive

We now generalize the above analysis to an rabi-frequency modulated transverse drive of the form

$$\Omega(t) = \frac{\Omega_0}{2}\left[1 + \cos(r\omega t)\right], \qquad r \in \mathbb{Z}. \tag{33}$$

The interaction-picture Hamiltonian becomes

$$H_I(t) = \frac{\Omega_0}{2} \sum_i \left[1 + \cos(r\omega t)\right] \left[\tilde{\sigma}_i^+ e^{+i\phi_i(t)} + \tilde{\sigma}_i^- e^{-i\phi_i(t)}\right], \tag{34}$$

where $\phi_i(t)$ is defined as in Eq. (S9),

$$\phi_i(t) = \alpha_i t + \frac{\Delta_0}{\omega}\sin(\omega t), \qquad \alpha_i = \sum_{j\in \mathrm{LR}(i)} V_{ij} n_j. \tag{35}$$

To first order in the interaction-picture Dyson expansion, the effective Floquet Hamiltonian is given by the time average

$$H_F^{(1)} = \frac{1}{T}\int_0^T H_I(t)\, dt, \qquad T = \frac{2\pi}{\omega}. \tag{36}$$

Substituting the expression for $H_I(t)$ and performing the time average yields

$$H_F^{(1)} = \frac{\Omega_0}{2} \sum_i \left[\tilde{\sigma}_i^+ \mathcal{I}_r(\alpha_i) + \tilde{\sigma}_i^- \mathcal{I}_r^*(\alpha_i)\right], \tag{37}$$

with

$$\mathcal{I}_r(\alpha) = \frac{1}{T}\int_0^T dt\ \left[1 + \cos(r\omega t)\right] e^{i[\alpha t + (\Delta_0/\omega)\sin(\omega t)]}. \tag{38}$$

To evaluate this integral, we again employ the Jacobi–Anger expansion

$$e^{i(\Delta_0/\omega)\sin(\omega t)} = \sum_{n=-\infty}^{\infty} J_n(\Delta_0/\omega)\, e^{in\omega t}. \tag{39}$$

Using $\cos(r\omega t) = (e^{ir\omega t} + e^{-ir\omega t})/2$, Eq. (38) becomes

$$\begin{aligned}\mathcal{I}_r(\alpha) = \frac{1}{T}\sum_{n=-\infty}^{\infty} J_n(\Delta_0/\omega)\int_0^T dt\; e^{i(\alpha+n\omega)t} \\ + \frac{1}{2T}\sum_{n=-\infty}^{\infty} J_n(\Delta_0/\omega)\int_0^T dt\;\left[e^{i(\alpha+(n+r)\omega)t} + e^{i(\alpha+(n-r)\omega)t}\right].\end{aligned} \tag{40}$$

Each time integral can be evaluated explicitly as

$$\int_0^T dt\; e^{i(\alpha+m\omega)t} = \frac{e^{i(\alpha+m\omega)T} - 1}{i(\alpha+m\omega)}, \tag{41}$$

which, using $T = 2\pi/\omega$ and $e^{im\omega T} = 1$ for integer m, simplifies to

$$\int_0^T dt\; e^{i(\alpha+m\omega)t} = \frac{e^{i2\pi\alpha/\omega} - 1}{i(\alpha+m\omega)}. \tag{42}$$

Collecting terms, we arrive at the closed-form expression

$$\mathcal{I}_r(\alpha) = \left(e^{i2\pi\alpha/\omega} - 1\right)\sum_{n=-\infty}^{\infty}\frac{J_n(\Delta_0/\omega)}{iT}\left[\frac{1}{\alpha+n\omega} + \frac{1}{2}\left(\frac{1}{\alpha+(n+r)\omega} + \frac{1}{\alpha+(n-r)\omega}\right)\right], \tag{43}$$

which reduces to the single-frequency result for $r = 0$.

Remarks

The amplitude modulation introduces additional near-resonant denominators at $\alpha \simeq \pm r\omega$, allowing multiple Floquet channels to contribute to the effective spin-flip amplitude. As discussed in the main text, this structure enables both enhancement and suppression of the effective transverse dynamics depending on the parity of r and the value of Δ_0/ω.

In the regime $|\alpha_i| \ll \omega$, the coefficient $\mathcal{I}_r(\alpha_i)$ appearing in the first-order Floquet Hamiltonian for the bifrequency drive admits an expansion of the form

$$\mathcal{I}_r(\alpha_i) = \mathcal{I}_r^{(0)} + \alpha_i\,\mathcal{I}_r^{(1)} + O(\alpha_i^2), \tag{44}$$

with

$$\mathcal{I}_r^{(0)} = J_0(\Delta_0/\omega) + \frac{1+(-1)^r}{2}\,J_r(\Delta_0/\omega), \tag{45}$$

and

$$\mathcal{I}_r^{(1)} = \sum_{n\neq 0,\pm r} J_n(\Delta_0/\omega)\left[\frac{1}{n\omega} + \frac{1}{2}\left(\frac{1}{(n+r)\omega} + \frac{1}{(n-r)\omega}\right)\right]. \tag{46}$$

As a result, the effective Floquet Hamiltonian contains a drive-renormalized constrained spin-flip term together with an interaction-induced density-assisted correction at linear order in V_{ij}.

IV. NUMERICAL SIMULATIONS

Numerical benchmarks for system sizes $L = 14$–16 employed two complementary approaches. Full quantum dynamics under the Rydberg Hamiltonian (Eq. 1 of main text) were computed using BLOQADE, an open-source python package from QuEra for simulating neutral-atom quantum processors. Simulations retained the complete van der Waals interaction $V_{ij} = C_6/r_{ij}^6$ between all atom pairs and employed identical time-discretized drive protocols as experiments.

For comparison with constrained models, we implemented PXP-type Hamiltonians that project out nearest-neighbor Rydberg excitations. Two variants were considered: PXP, which forbids only nearest-neighbor double occupancy, and extended-PXP (PPXPP), which additionally constrains next-nearest neighbors [3]. Time evolution employed second-order Trotterization with 400 steps per drive cycle, yielding relative errors below 10^{-3}. All simulations discussed in the main text employed open boundary conditions matching experimental geometries. Thus only parity symmetry was exploited to reduce computational cost, no other approximations were imposed.

However, system sizes up to $L = 36$ were numerically accessible for certain geometries, boundary conditions, and parameter regimes, and we present representative results in these regimes in this section. We note that in some parameter regimes, simulations predict excitation densities below 1% at destructive interference points. In such cases, experimental state preparation and measurement (SPAM) errors ($\epsilon_{\mathrm{det},g} \approx 0.01$) would dominate the signal. The parameters presented in the main text were therefore chosen to balance interference visibility with experimental observability, typically ensuring $n(T) \gtrsim 0.02$ at destructive minima.

A. Initial state dependence

In this section, we investigate the dependence of temporal freezing on the choice of initial state. This provides a further probe of the genuinely many-body character of the phenomenon, as the system response is no longer determined solely by the drive protocol but also by the structure of correlations encoded in the initial state. We restrict attention here to exact numerical simulations within the constrained PXP model, which allows us to systematically explore a range of highly nontrivial initial conditions. Experimental implementation of such state-dependent protocols is left for future work.

Complementing the vacuum state considered in the main text, we study the following three initial states:

$$\begin{aligned} \text{Single Rydberg excitation} &: |1\rangle \equiv |1000\cdots\rangle \\ \text{Néel state} &: |\mathbb{Z}_2\rangle \equiv |1010\cdots\rangle \\ \mathbb{Z}_3 \text{ state} &: |\mathbb{Z}_3\rangle \equiv |100100\cdots\rangle\,. \end{aligned} \tag{47}$$

The $|\mathbb{Z}_2\rangle$ state is well known to exhibit quantum many-body scar (QMBS)-induced long-lived oscillations of local observables [4]. The $|\mathbb{Z}_3\rangle$ state displays similar behavior, albeit with reduced coherence, and can be prepared as the ground state of a Rydberg Hamiltonian with large negative detuning and blockade radius equal to two lattice spacings, a regime associated with non-Ising critical points [3].

In Fig. 3 we plot $\ln(1-\mathcal{F}(T))$, where $\mathcal{F}(T) = |\langle\psi_0|\psi(T)\rangle|^2$, together with the excitation density $n(T)$ as functions of drive frequency for all three initial states. Minima of $\ln(1-\mathcal{F}(T))$ correspond to strongest freezing. For the single-excitation state $|1\rangle$, the locations of the freezing points closely match those found for the vacuum state. By contrast, the $\mathbb{Z}_2$ and $\mathbb{Z}_3$ states exhibit maxima of $n(T)$ at the same frequencies, reflecting a qualitatively different response to the drive.

For the $|\mathbb{Z}_2\rangle$ state this behavior is expected, as it already maximizes the allowed Rydberg excitation density within the constrained Hilbert space. The response of the $|\mathbb{Z}_3\rangle$ state is more subtle, since the drive does not generate states with higher excitation density. In both these scenarios the dynamical freezing manifests through enhanced fidelity. Overall, these results demonstrate that temporal freezing and its enhancement under bifrequency driving persist well beyond the vacuum sector, with the precise locations and strengths of freezing depending weakly but systematically on the initial state. Interestingly, the fidelity at freezing points is often higher for the correlated initial states considered here than for the vacuum, suggesting that initial many-body correlations can further stabilize interference-induced freezing. The experimental realization of such correlated initial states requires substantial additional preparation overhead and was therefore not pursued in the present work.

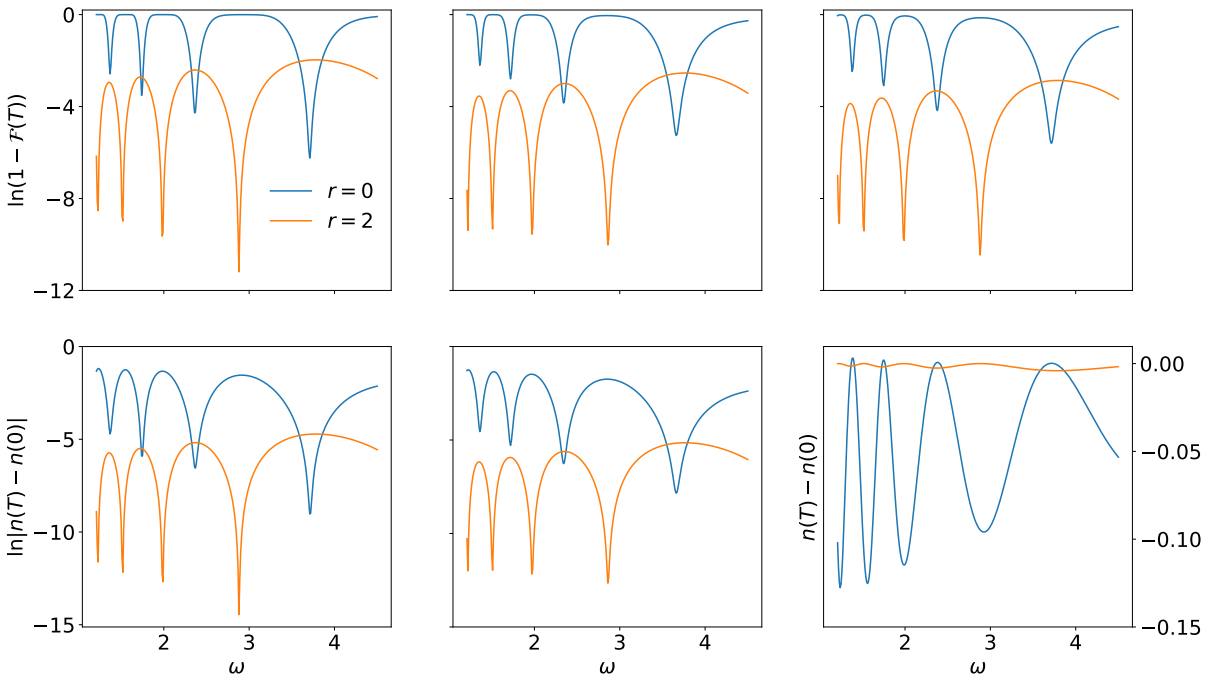

FIG. 3. **Initial state dependence :** Behavior of Fidelity, $\mathcal{F}(T)$(upper panels) and $n(T)$ (lower panels) for the initial states $|1\rangle$ (left panels), $\mathbb{Z}_2$ (middle panels) and $\mathbb{Z}_3$ (right panels). See text for details. $N = 14$, $\Delta_0 = 20$, $\Omega_0 = 2$.

B. Dependence on system size, boundary conditions and ratio of drive frequencies

In this section we examine the robustness of the freezing phenomenon with respect to system size, boundary conditions, and the ratio of the two drive frequencies. To access larger system sizes within exact diagonalization, we exploit all available lattice symmetries, resolving translations along both spatial directions, reflections about the x and y axes, and inversion with respect to the diagonal of the square lattice. This symmetry resolution reduces the effective Hilbert space dimension by a factor of order $\sim 8L_xL_y$. For instance, restricting to the sector $K_x = 0$, $K_y = 0$, $I_x = +1$, $I_y = +1$, $I_d = +1$ yields a matrix of dimension 9702 for a 6×6 lattice, compared to a full constrained Hilbert space dimension of 2 406 862.

We find that increasing system size leads to both a slight shift of the freezing minima toward higher frequencies and a reduction in the overall degree of freezing, as illustrated by the comparison between 4×4 and 6×6 lattices in Fig. 4 (left panel). This trend suggests that finite-size effects play a quantitative role in stabilizing interference-induced freezing, while the fate of the phenomenon in the thermodynamic limit remains an open question.

We further observe that the locations of the freezing minima are insensitive to the choice of boundary conditions, as shown in Fig. 4 (middle panel). This is encouraging from an experimental perspective, as open boundary conditions are most naturally implemented in current quantum simulation platforms. Finally, we investigate the dependence on the ratio r of the two drive frequencies (Fig. 4, right panel). Among the cases studied, $r = 2$ is distinguished by consistently higher fidelity over a broad frequency range, indicating a particularly robust interference condition. A deeper microscopic understanding of why $r = 2$ is particularly robust, beyond the effective Bessel interference picture presented here, remains an open direction for future theoretical work.

V. EXCITATION DENSITY DISTRIBUTION

In the main text we characterized the system response using the Rydberg excitation density $n(T)$ averaged over all atoms in a particular configuration as a function of the driving frequency. This global observable efficiently captures the emergence of non-equilibrium interference effects, including the appearance of freezing points and enhanced exci-

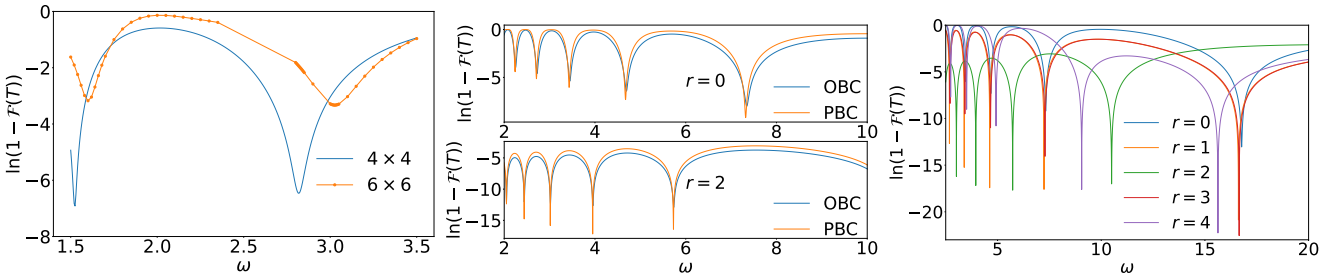

FIG. 4. **System size dependence (Left) :** Fidelity ($\mathcal{F}(T)$) for 4×4 and 6×6 square lattices. $\Delta_0 = 10$, $\Omega_0 = 2$, $r = 2$. **Dependence on boundary conditions (middle) :** $\mathcal{F}(T)$) for 4×4 lattice with periodic (open) boundary conditions (PBC (OBC)). $\Delta_0 = 40$. **r-dependence (Right) :** $\mathcal{F}(T)$) for 4×4 lattice. $\Delta_0 = 40$. Here, we start from the initial ground state of the Hamiltonian.

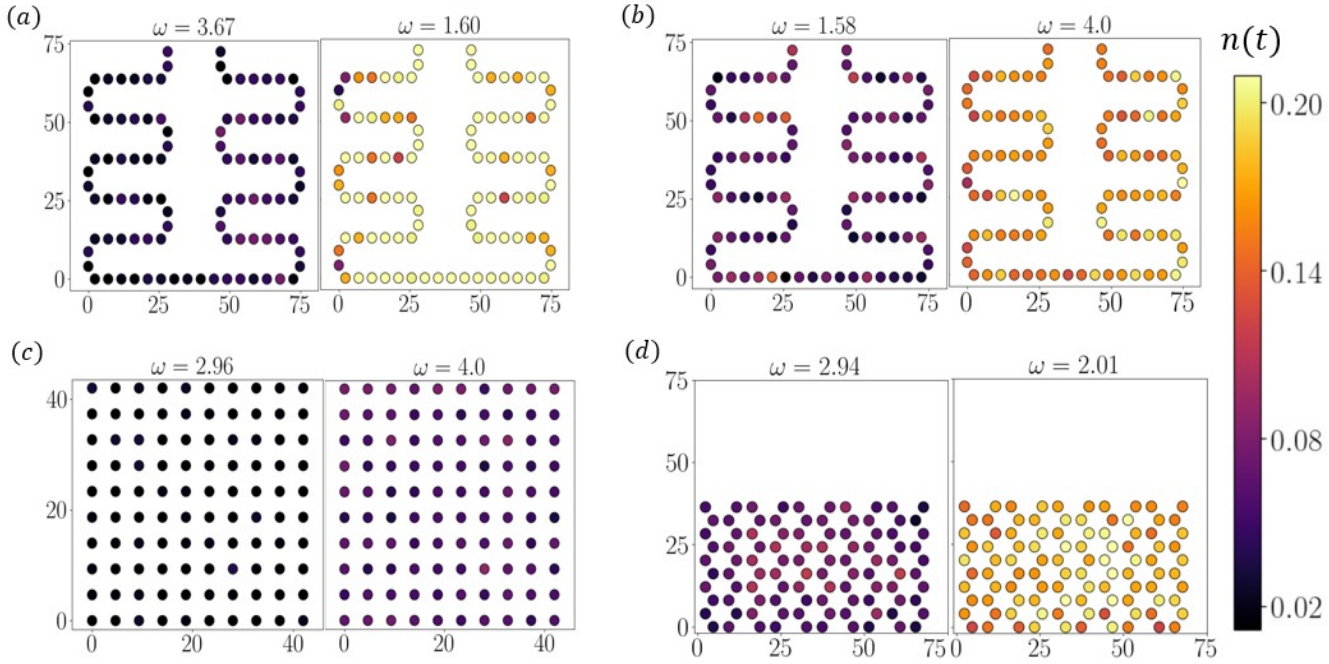

FIG. 5. **Local Rydberg excitation probability of each individual atom:** Fig.5 (a),(b) corresponds to single- and bi-frequency driving respectively for one-dimensional chains (represented by the snake configuration). (c) Shows the bi-frequency result for two-dimensional square lattice showing that the excitation is suppressed even at the frequencies where we have the peak, and (d) shows the bi-frequency result for two-dimensional hexagonal lattice. For all the figures, Left: Frequencies corresponding to the freezing points, and Right: frequencies at which the total excitation density is maximized (right). The frequencies are mentioned at the top of each plot.

tation regimes, and allows for a direct comparison across different system geometries and driving protocols. However, such spatial averaging necessarily masks the underlying site-resolved structure of the many-body excitation patterns that develop during the driven dynamics.

Here, we therefore complement the averaged analysis by presenting the local Rydberg excitation probability of each individual atom different lattice geometries and driving protocols. Fig. 5 (a),(b) corresponds to single- and bi-frequency driving for one-dimensional chains (represented by the snake configuration). The bi-frequency driving for two-dimensional square and hexagonal geometries are shown in Fig. 5 (c) and (d) respectively. We choose two representative driving frequencies for Fig. 5(a,b,c,d): (i) frequencies corresponding to the freezing points (left), and (ii) frequencies at which the total excitation density is maximized (right). Fig. 6 represents the effect of changing the interatomic distance for the same geometry at $\omega \sim 2.5 rad/\mu s$. By resolving the excitation distribution at the single-site level, we demonstrate that the observed extrema in the averaged excitation are not the result of localized or edge-dominated effects, but instead arise from a highly coherent and spatially homogeneous excitation pattern across the entire atomic configuration.

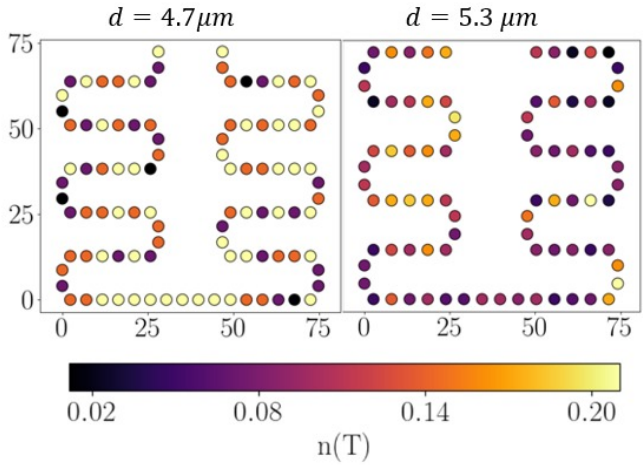

FIG. 6. **Local Rydberg excitation probability of each individual atom demonstrating effect of inter-atomic distance:** This plot represents the effect of changing the interatomic distance for the same geometry at $\omega \sim 2.5\ rad/\mu s$. It demonstrate that at $d = 5.3\mu m$ the excitations are more suppressed compared to that at $d = 4.7\mu m$ for the same frequency.

At both the freezing points and the excitation maxima, the site-resolved excitation probabilities remain approximately uniform across most atoms. Modest deviations are observed in regions of local geometric variation, such as near the bends of the snake-like configuration. These deviations do not result in any abrupt redistribution of the overall excitation density toward higher or lower values.

The observed spatial variations arise from interaction effects and reflect local geometric constraints. Their systematic presence across different geometries and driving protocols indicates that the non-equilibrium features discussed in the main text are collective in origin rather than dominated by local inhomogeneities. The site-resolved data therefore support the interpretation of these features as global many-body effects in driven Rydberg systems.

[1] R. Mukherjee, H. Guo, and D. Chowdhury, Floquet thermalization via instantons near dynamical freezing, Phys. Rev. X **16**, 011041 (2026).
[2] R. Ghosh, B. Mukherjee, and K. Sengupta, Floquet perturbation theory for periodically driven weakly interacting fermions, Phys. Rev. B **102**, 235114 (2020).
[3] R. Ghosh, A. Sen, and K. Sengupta, Ramp and periodic dynamics across non-ising critical points, Phys. Rev. B **97**, 014309 (2018).
[4] C. J. Turner, A. A. Michailidis, D. A. Abanin, M. Serbyn, and Z. Papić, Weak ergodicity breaking from quantum many-body scars, Nature Physics **14**, 745 (2018).